



JGR Space Physics

RESEARCH ARTICLE

10.1029/2023JA031513

Key Points:

- Electron temperature enhancement occurs at night and is prominent in the 260°–360°E (80°–280°E) longitude region in the NH (SH) winter
- Low-energy electrons (<100 eV)
 associated conjugate photoelectron
 and local electron density variation
 can contribute to the enhancement
- Its global distribution is determined by the geomagnetic field configuration and terminator around the two magnetic conjugate points

Correspondence to:

J. Xu and Q. Zhang, jyxu@spaceweather.ac.cn; zhangqinghe@sdu.edu.cn

Citation:

Liang, J., Xu, J., Zhang, Q., Liu, J., Zhang, Y., Zhang, S.-R., et al. (2023). Global distribution of electron temperature enhancement at mid-low latitudes observed by DMSP F16 satellite. *Journal of Geophysical Research: Space Physics, 128*, e2023JA031513. https://doi.org/10.1029/2023JA031513

Received 22 MAR 2023 Accepted 17 AUG 2023

Global Distribution of Electron Temperature Enhancement at Mid-Low Latitudes Observed by DMSP F16 Satellite

Jianyun Liang^{1,2}, Jiyao Xu^{1,2}, Qinghe Zhang³, Jing Liu³, Yongliang Zhang⁴, Shun-Rong Zhang⁵, Xiangyu Wang³, Zanyang Xing³, and Kun Wu⁶

¹State Key Laboratory of Space Weather, National Space Science Center, Chinese Academy of Sciences, Beijing, China, ²University of Chinese Academy of Sciences, Beijing, China, ³Shandong Provincial Key Laboratory of Optical Astronomy and Solar-Terrestrial Environment, Institute of Space Sciences, Shandong University, Weihai, China, ⁴The Johns Hopkins University Applied Physics Laboratory, Laurel, MD, USA, ⁵Haystack Observatory, Massachusetts Institute of Technology, Westford, MA, USA, ⁶High Altitude Observatory, National Center for Atmospheric Research, Boulder, CO, USA

Abstract This study investigates the global distribution of electron temperature enhancement observed by Defense Meteorological Satellite Program F16 satellite and its dependence on the season and solar activity for the solar maximum (2014) and minimum (2018) years during geomagnetic quiet times (maximum per day ap <10). Electron temperature enhancements occurred mainly over the North American-Atlantic (260°–360°E) and Eurasia (0°–160°E) (Southern Oceania (80°–280°E)) sector in the Northern (Southern) Hemisphere and are prominent in the winter hemispheres and solar maximum year. They have obvious longitude characteristics. Interestingly, they could extend to geomagnetic equatorial regions in the North American-Atlantic sector from high to low latitudes in the December Solstice, further crossed the magnetic equator, and merged into the Southern Hemisphere in 2014, where the maximum temperature reached ~3500 K. Our analysis indicates that low-energy electrons (<100 eV) associated with photoelectron from the conjugate sunlit hemisphere, can contribute to these enhancements. Furthermore, the local geomagnetic declination, magnetic equator position, and terminator position at magnetic conjugate points together can impact the global distribution of photoelectrons of different energies and therefore the electron temperature enhancement distribution. Other processes (including local electron density variation) may play certain roles as well.

Plain Language Summary Photoelectrons are supra-thermal low-energy electrons in the sunlit hemisphere that can move to the nightside hemisphere along the magnetic field lines and heat the thermal electrons around the conjugate location, which causes the electron temperature anomalous enhancement and re-distribution of electron temperature at mid-low latitudes on nightside. The global distribution characteristics, seasonality, and solar activity of the electron temperature enhancement were studied using in-situ DMSP F16 satellite plasma, energy particle precipitation, and geomagnetic field observations in 2014 and 2018 during geomagnetic quiet times. It is shown that the electron temperature enhancement is prominent in the Northern Atlantic (260°–360°E) (the Southern Oceania (80°–280°E)) sector in the Northern (Southern) Hemisphere winter and is more visible during a solar maximum year. Furthermore, the geomagnetic field configuration and the solar terminator around the two magnetic conjugate points modulate the photoelectron precipitated positions in the conjugate night hemisphere, and the magnetic field line length and intensity between the two magnetic conjugate points may determine the flux of the photoelectron precipitation, which all affect the global distribution of the electron temperature enhancement. Other factors, including electron density, which controls the cooling of electrons, could also impact the electron temperature under certain conditions.

1. Introduction

The sunrise time is not always the same at different latitudes, and the magnetic field lines and solar terminator orientation also do not always coincide. Therefore, photoelectrons (PEs) in the sunlit hemisphere, which are generated by the photoionization of neutral atoms and molecules caused by the solar extreme ultraviolet (EUV) radiation (Brace et al., 1963; Shawhan et al., 1970), will move to the night hemisphere (i.e., conjugate photoelectrons (CPs)) along the magnetic field line and heat the ambient electrons causing the electron temperature enhancement on nightside (Hanson, 1963; Kwei, 1967; Nagy et al., 1969) that is a higher electron temperature than its background. Monitoring the heating effect of CPs on the night ionosphere also helps us to understand the impact of the geomagnetic field on the distribution of night ionospheric electron temperature.

© 2023. American Geophysical Union. All Rights Reserved.

LIANG ET AL. 1 of 13

As early as the 1960s, the electron temperature enhancement at an altitude range of 225–375 km was observed before sunrise in winter by the incoherent scatter radar in Arecibo (Carlson, 1966, 1968). This phenomenon was also observed at an altitude of ~375 km in winter by the incoherent scattering radar at Millstone Hill and Saint-Santin, France (Carru et al., 1967; Evans, 1967, 1968). Since then, pre-dawn ionospheric heating has also been observed in the North American sector at the altitudes of the Injun 5, ROC-SAT-1, and Hinotori satellites; however, there is no similar phenomenon in the Eurasia sector (Burke et al., 1979; Chao et al., 2003; Kakinami et al., 2010; Kil et al., 2022; Oyama et al., 1997). There are also many comparative studies based on theoretical calculations and the observations by radars, satellites, and rockets (Duboin, et al., 1968; Evans & Gastman, 1970; Kwei & Nisbet, 1966, 1968; Mukai et al., 1979; Rao & Maier, 1970). These studies verified that the downward heat flux heating electrons along the magnetic field line in the nightside hemisphere is approximately the same as that of PEs from the conjugate sunlit hemisphere along the magnetic field line. In recent years, there have also been studies on the influence of the geomagnetic field configuration on the CPs distribution (Kakinami et al., 2010; Kil et al., 2020; Solomon et al., 2020). These studies confirmed that the electron temperature enhancement is caused by PEs heating from the conjugate sunlit hemisphere based on the observation at a single station or a low-latitude sector.

However, there is still a lack of study on the global distribution characteristics of electron temperature enhancement, its seasonality, solar activity, and the modulation effect of the geomagnetic field on its distributions. To investigate these issues, we analyzed the plasma, energy particle precipitation, and geomagnetic field data of Defense Meteorological Satellite Program (DMSP) F16 in the solar maximum (minimum) year during geomagnetic quiet times. Section 2 describes the data and methodology used in this study. The global distribution characteristics, seasonality, and solar activity of the electron temperature enhancement are described in Section 3. Section 4 discusses the potential physical mechanisms of electron temperature enhancement and the factors that modulate its distribution. Section 5 presents the conclusions of this study.

2. Data Sources and Methodology

The DMSP F16 satellite, launched on 18 October 2003, operates in a sun-synchronous polar orbit with an orbital inclination of 98° at an 835–860 km altitude and an orbital period of ~101 min. The onboard instruments include Special Sensor for Ions, Electrons, and Scintillation (SSIEs) that offers the data of ion horizontal cross-track and vertical velocity, the Retarding Potential Analyzer data of hydrogen and helium ions, oxygen ions, total ion density, and ion temperature, and the Electron Langmuir Probe (EP) data of electron temperature and density, Special Sensor for Particle Flux (SSJ/5) that offers the count of precipitating electrons and ions within an energy range of 30 eV–30 keV, and Fluxgate Magnetometer (SSM) that offers the magnitude of the local magnetic field (Daniel et al., 2014; Delorey et al., 1989; Hardy et al., 1984; Rich, 2001). Electron temperature from the EP mode of SSIEs with 4-s resolution, precipitating electron differential flux from SSJ/5, and the local magnetic field from SSM with 1-s resolution are used in this study (https://www.ncei.noaa.gov/data/dmsp-space-weather-sensors/access/).

The data for geomagnetic inclination, declination, and three-dimensional magnetic field lines are obtained from the International Geomagnetic Reference Field of the thirteenth generation (IGRF13) (https://www.ngdc.noaa.gov/IAGA/vmod/igrf.html).

The DMSP F16 satellite solar local times (LTs) of the ascending (descending) orbit at the equator have changed from 08:00LT (20:00LT) in 2004 to 04:00LT (16:00LT) in 2020 due to orbital precession. We chose the data in the solar maximum year 2014 (05:00LT) and the solar minimum year 2018 (04:00LT), which are the night orbits at mid-low latitudes with relatively pure "cold" background temperature between after midnight and before sunrise, during geomagnetic quiet time (maximum per day ap < 10) to study electron temperature enhancement. The other LTs of DMSP F16 either are after dusk, that complex background temperature affected by the previous "hot" background due to prolonged photoionization and recombination on daytime, or have already entered the day affected by illumination. So, we will not consider these LTs here. These data were binned and averaged on $5^{\circ} \times 5^{\circ}$ longitude-latitude grids when there were more than 50 valid data samples in a grid. Otherwise, the grid would be filled with blanks. We also divided all data into different seasons corresponding to the March Equinox (February, March, and April), the June Solstice (May, June, and July), the September Equinox (August, September, and October), and the December Solstice (November, December, and January).

LIANG ET AL. 2 of 13

wiley.com/doi/10.1029/2023JA031513 by Massachusetts Institute of Technolo.

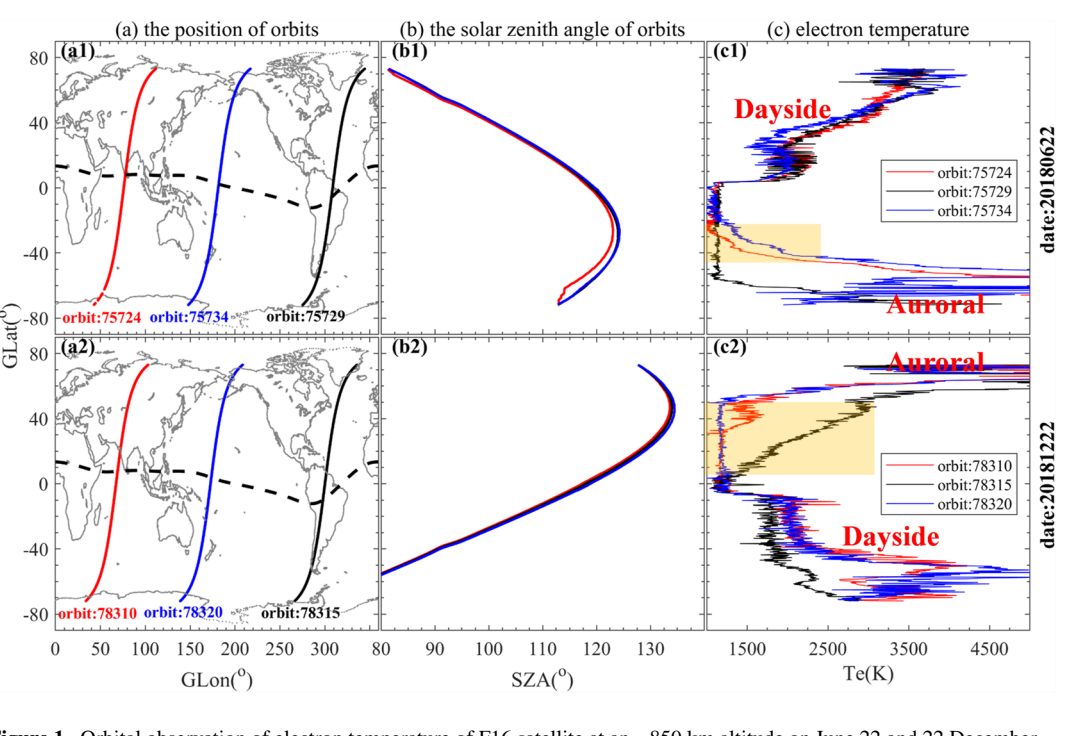


Figure 1. Orbital observation of electron temperature of F16 satellite at an ~850 km altitude on June 22 and 22 December 2018. From left to right, Panels are the orbit position in different sectors (a), the Solar Zenith Angle (SZA) (b) and the electron temperature (c) in these orbits, respectively. The red, blue, and black lines are in the Eurasia, Northern Pacific, and Northern Atlantic sectors, respectively. The electron temperature enhancement on orbit 75724 (78315) and 75729 (78310) in the SH (NH) are indicated by orange shadings.

3. Observation Results

The F16 satellite orbits and electron temperature data at an 850 km altitude are shown in Figure 1 in two seasons in 2018, June 22 and December 22. There is a noticeable electron temperature rise at mid-low latitude on nightside in orbits 75724 and 75734 (78310 and 78315) compared with orbit 75729 (78320) in the winter hemisphere (Orange shaded region in Figures 1c1 and 1c2). The aurora region is where the winter hemisphere exhibits significantly higher electron temperatures. The sharp electron temperature rising at 118° SZA during darkness in the summer hemisphere is not a true ionospheric variation due to photoelectron contamination collected by the electron probe when the satellite orbit would move to the sunlit. Furthermore, the temperature at the latitude of less than 118° SZA on the orbit is higher than the true value. The photoelectron contamination influence on DMSP measurements decreased toward the solar maximum years (Green, 2001). This contamination was almost absent in 2014. Although this contamination in 2018 cannot be ruled out at SZA $\leq 118^{\circ}$, fortunately, the electron temperature enhancement at mid-low latitudes on nightside is not within the latitude range of this contamination. The electron temperature enhancement has a special global distribution and a strong dependence on local time (LT), season, and solar activity, which were derived as the seasonal average of the electron temperature observed by F16 during the magnetic quiet period in 2014 (~5LT) and 2018 (~4LT). This enhancement region in the winter hemisphere is marked with the red arrow in Figure 2.

3.1. Global Distribution Characteristics of Electron Temperature Enhancement

The global distribution of electron temperature enhancement exhibits a considerable longitudinal difference. In the NH, the electron temperature enhancement mainly occurred near the Eurasia sector $(0^{\circ}-160^{\circ}E)$ and North American-Atlantic sector $(260^{\circ}-360^{\circ}E)$ in the December Solstice (Figure 2a4) and the March and September Equinox (Figures 2a1 and 2a3). It exhibited behavior that crossed the magnetic equator and extended into the SH in the Atlantic sector in the December Solstice of 2014 (Figure 2a4), but only to low magnetic latitudes in the Eurasia sector. The electron temperature in the Atlantic sector was \sim 1600 and \sim 600 K higher than those in the Pacific and Eurasia sectors, respectively. The most intense electron temperature enhancement occurred in the Northern Atlantic sector, weakened in the Eurasia sector, and was weakest in the Northern Pacific sector. In the SH, the electron temperature enhancement was primarily located in the Southern Oceania sector $(80^{\circ}-280^{\circ}E)$

LIANG ET AL. 3 of 13

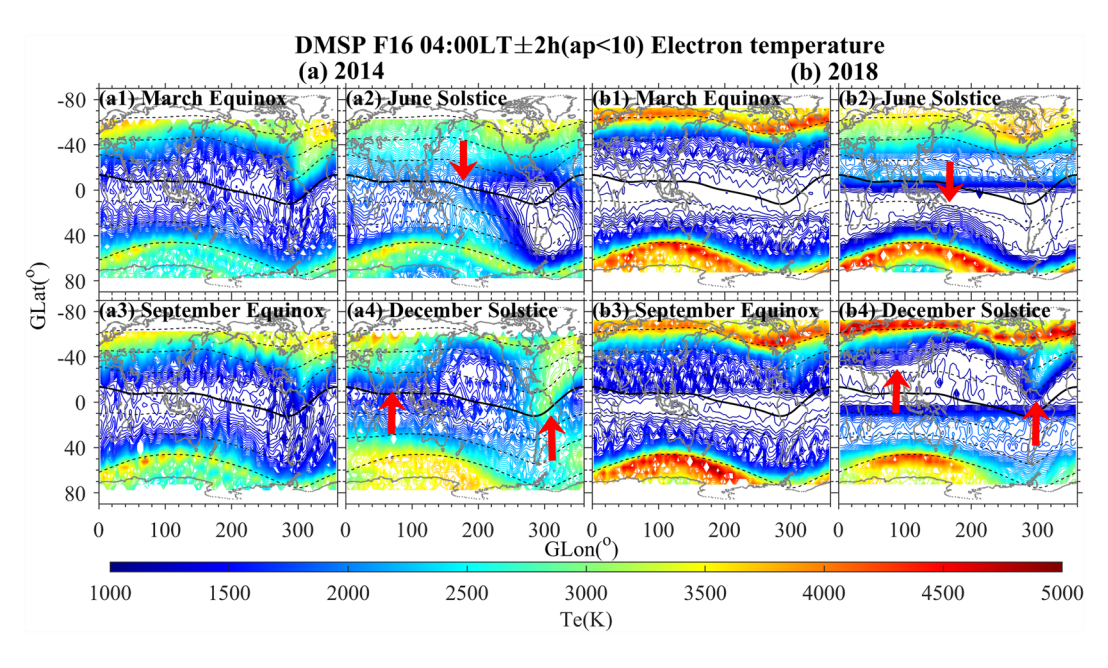


Figure 2. The electron temperature enhancement distribution during geomagnetic quiet times in (a) 2014 and (b) 2018. The black line denotes the magnetic latitude line at 20° intervals, and the red arrow is for marking the electron temperature enhancement in the winter hemisphere.

in the June Solstice (Figure 2a2) and the March and September Equinox (Figures 2a1 and 2a3) of 2014. It still had the behavior of crossing the magnetic equator in the Southern Oceania sector in the June Solstice of 2014 (Figure 2a2). But the temperature is ~1000 K lower than that in the NH. Moreover, the longitudinal difference was not clear compared with the NH (Figure 2a4). As a result, the electron temperature enhancement is more noticeable in the Northern Atlantic (Southern Oceania) sector in the NH (SH).

3.2. Dependence on Seasons and Solar Activity of Electron Temperature Enhancement

The electron temperature enhancement is strongly dependent on seasons. Compared with the December Solstice of 2014 (Figure 2a4), the electron temperature enhancement region had shrunk around the magnetic equator in the Atlantic, around middle magnetic latitudes in the Eurasia (Southern Oceania) sector of NH (SH) in the March (September) Equinox of 2014 (Figures 2a1 and 2a3). Whether in the NH or SH, the latitudinal extension and temperature in the electron temperature enhancement region in the Equinox were weaker than in the Solstice. Thus, electron temperature enhancement both in the NH and SH are more pronounced in the Solstice.

The longitude-latitude spatial span and temperature in the electron temperature enhancement regions are considerably different between the solar maximum and minimum years. Compared with 2014 (Panel (a) in Figure 2), the electron temperature enhancement region in 2018 (Panel (b) in Figure 2) shrank to a high magnetic latitude. It had gone back to low magnetic latitudes from the SH in the Atlantic sector and to the middle from low magnetic latitudes in the Eurasian sector of NH in the December Solstice of 2018 (Figure 2b4). Electron temperature enhancement in the SH in the June Solstice of 2018 (Figure 2b2) also shrank to a high magnetic latitude, but this contraction was not comparable to that in the NH. The longitude width in 2014 was wider than in 2018, particularly in the NH in the December Solstice. The maximum width was 260°. In addition, the temperature in the electron temperature enhancement region in 2014 (Panel (a) in Figure 2) was much higher than that in 2018 (Panel (b) in Figure 2), regardless of the seasons. Therefore, electron temperature enhancement in the solar maximum year has a considerably wider longitude-latitude span and higher temperature.

4. Discussion

4.1. What Is the Source of Electron Temperature Enhancement?

In general, the F region electron temperature is governed by the balance of heating through PEs, CPs, soft electron (<1 keV) precipitation, heat conduction along magnetic field lines from the plasmasphere, and cooling

LIANG ET AL. 4 of 13

through collisions with neutrals and ions (Geisler & Bowhill, 1965; Schunk & Nagy, 1978; Su et al., 1999; Watanabe et al., 1995). At 04:00/05:00 LT and mid-low latitude, there was no solar EUV irradiance to generate local PEs. Moreover, on nightside, soft electrons from the magnetosphere are typically precipitated in the polar region (Meng, 1976; Newell et al., 1996, 2004). The heat conduction of the plasmasphere at mid-low latitudes is restrained due to the close to horizontal magnetic field lines (Kil et al., 2022). The cooling via the electron energy loss through the Coulomb ion-electron collision is proportional to the square of the electron density (Bilitza et al., 2007). With low density, the electron energy cannot be efficiently transferred to ambient ions; therefore, electron temperature tends to be high. In the absence of external heating exchange, the same heat capacity of electrons would imply that low electron density corresponds to high electron temperature. In other words, the electron temperature is strongly affected by the variation in electron density. Therefore, the heating of CP between the two conjugated hemispheres along the magnetic field line and the effect of electron density may be closely related to the electron temperature enhancement at mid-low latitude on nightside.

To understand the role of CPs, we first considered the electron differential energy flux (JE_i) in the low-energy channel (only 30, 65, and 139 eV are shown) of the DMSP F16 satellite during geomagnetic quiet times in 2014 and 2018. Then we use the average electron temperature of F15 satellite (~3LT at an earlier moment than F16) observations at mid-low magnetic latitude ($-60 \sim 0/0 \sim 60^{\circ}$ MLAT), by which the electron temperature enhancement is barely observed, as the background temperature. Next, we find the position where the electron temperature satisfies the equation of (Te-Te_{F15})/Te_{F15} = 10% is taken as a rough reference boundary of electron temperature enhance zone in each hemisphere to reveal the relationship between the low-energy electron precipitation and electron temperature enhancement. The value of 10% is arbitrary; however, the contour highlights the longitudinal profile of the enhancement zone. A different value will result in a similar longitudinal profile with a shift in latitude. It is worth noting that the SSJ/5 sensors aboard the DMSP F16 satellite are easily to trap MeV electrons and protons and get counted when the satellite passes through Southeast South America (SAA, where energetic particles from the inner radiation belt increase the local particle flux, owing to the weakened geomagnetic field) (Anderson et al., 2018). The electron differential flux is $>0.2 \times 10^6$ in the grid of 150° W < longitude $< 50^{\circ}$ E and 50° S < latitude $< 15^{\circ}$ N (refer to IGRF 13) was set to "NaN" to eliminate the impact of SAA.

The distribution of low-energy electron precipitation at mid-low latitudes is strongly consistent with electron temperature enhancement. Regardless of the season in 2014 or 2018 (Panels (a) and (b) in Figures 3 and 4), the electron temperature enhancement reference boundary (magenta lines) coincides with the precipitation positions of 30 and 65 eV at mid-low latitudes, especially in the Solstice. Moreover, comparing Figures 4a4 and 2b4, the high temperature in the electron temperature enhancement region corresponds to high differential energy flux for the fixed electron energy. The most electrons energy in the electron temperature enhancement region is mostly less than 100 eV, which is in agreement with previous studies of the energy of CPs (Kwei & Nisbet, 1968; Mukai et al., 1979; Nagy & Banks, 1970; Rao & Maier, 1970). The electron differential energy flux distribution in the NH in the March and September Equinox of 2014 (Figures 3a1 and 3a3) were somewhat different from the electron temperature enhancement distribution, perhaps because the sources of low-energy electrons in the night hemisphere in the solar maximum years were more complex. Also, it is not only PEs that contribute to electron temperature enhancements. But there was still good consistency in the North American sector. The puzzling point is that the differential energy flux of energy electrons precipitation observed by F16 satellite in the NH (summer) hemisphere in the June Solstice of 2014 in Figures 3a2–3c2 is significantly weaker than that in the SH (winter) hemisphere.

In addition, we also determined the CPs distribution. PE in the sunlit hemisphere can reach the conjugate night hemisphere under the following conditions, as demonstrated in cartons in Figure 8a1. (a) An angle between the magnetic field line and terminator exists. No CP will reach the night hemisphere if the terminator is nearly parallel to the magnetic field line. (b) The magnetic foot pairs are on the dayside (green triangle) and nightside (magenta triangle), respectively. When the magnetic foot falls on the terminator (green star), the corresponding conjugate magnetic foot (magenta star) is the lowest latitude that CP can reach. Next, we would examine whether there was CP precipitation at the magnetic foot point the satellite passed through to give the CP and PE distribution in all orbits. Then we further observed whether the CP distribution matched the observed electron temperature enhancement and 30 eV electron differential energy flux distribution. Figure 5 reveals the results of the NH in the December Solstice of 2014 and 2018; both the distributions of electron temperature enhancement (Figure 5a) and 30 eV electrons differential energy flux (Figure 5b) can be well represented by the blue solid line (CP distribution). Moreover, the blue solid line is in good agreement with the electron temperature enhancement reference

LIANG ET AL. 5 of 13

from https://agupubs.onlinelibrary.wiley.com/doi/10.1029/2023J A031513 by Massachusetts Institute of Technolo, Wiley Online Library on [01/09/2023]. See the Terms and Conditions (https://onlinelibrary.

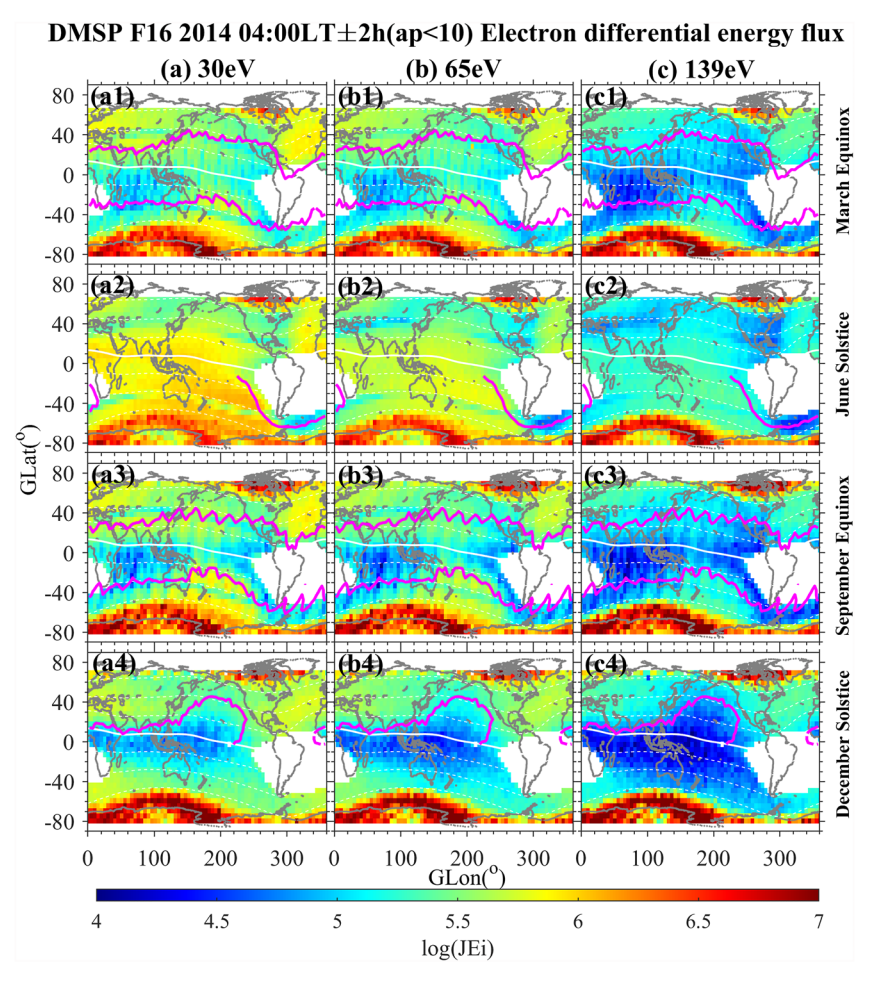


Figure 3. Relationship between electron differential energy flux (JEi) and electron temperature enhancement during the geomagnetic quiet times in 2014. The panels are (a) 30 eV, (b) 65 eV, and (c) 139 eV. The magenta lines are the electron temperature enhancement reference boundary. The white lines are the same as the black line in Figure 2.

boundary (magenta solid line) in Figure 5c. It is worth emphasizing that the electron temperature enhancement in the winter hemisphere in 2014 across the magnetic equator to the summer hemisphere is not only caused by the CP effect. The convergence of CP and PE distributions in Figure 5c2 in the North American-Atlantic sector could reveal that this sector's electron temperature enhancement distribution is no longer just the magnetic conjugate effect. Figure 8c illustrates the crossing equator physical schematic diagram of electron temperature enhancement in the NH on 22 December 2014. The orientation of the terminator (yellow solid line) on dayside and its conjugate position (yellow dotted line) on nightside could be determined when the satellite flew over the 310°E meridian of the Northern Atlantic Ocean in Figure 8c. The intersection of the longitude line and terminator in 2014 (white dot in Figure 8c) was above the magnetic equator than that in 2018 (white dot in Figure 8a2), because the precession of F16 satellite in 2014 was 1 hr later than that in 2018. Furthermore, the white line had all entered the day, while the orange line at night was all the area that CP could reach. In other words, the nightside region in the NH can be covered by CP (orange line) and merged into the dayside region affected by local PEs (white line). This combined CP and local PE effect, which changes as a function of latitude, is essentially consistent with the observed pattern of electron temperature enhancement at low latitudes. Besides that, 130.4 nm anomalous radiation measured by DMSP F16 satellite which is also caused by CPs, could also be observed in the electron temperature enhancement region (Kil et al., 2020).

Another important factor is the effect of electron density, as briefly noted in Section 4.1. In 2014 and 2018, the relationship between electron temperature and density in the electron temperature enhancement region was very different. It was relatively simple for 2014. The electron temperature enhancement region in the March

LIANG ET AL. 6 of 13

from https://agupubs.onlinelibrary.wiley.com/doi/10.1029/2023JA031513 by Massachusetts Institute of Technolo, Wiley Online Library on [01/09/2023]. See the Terms

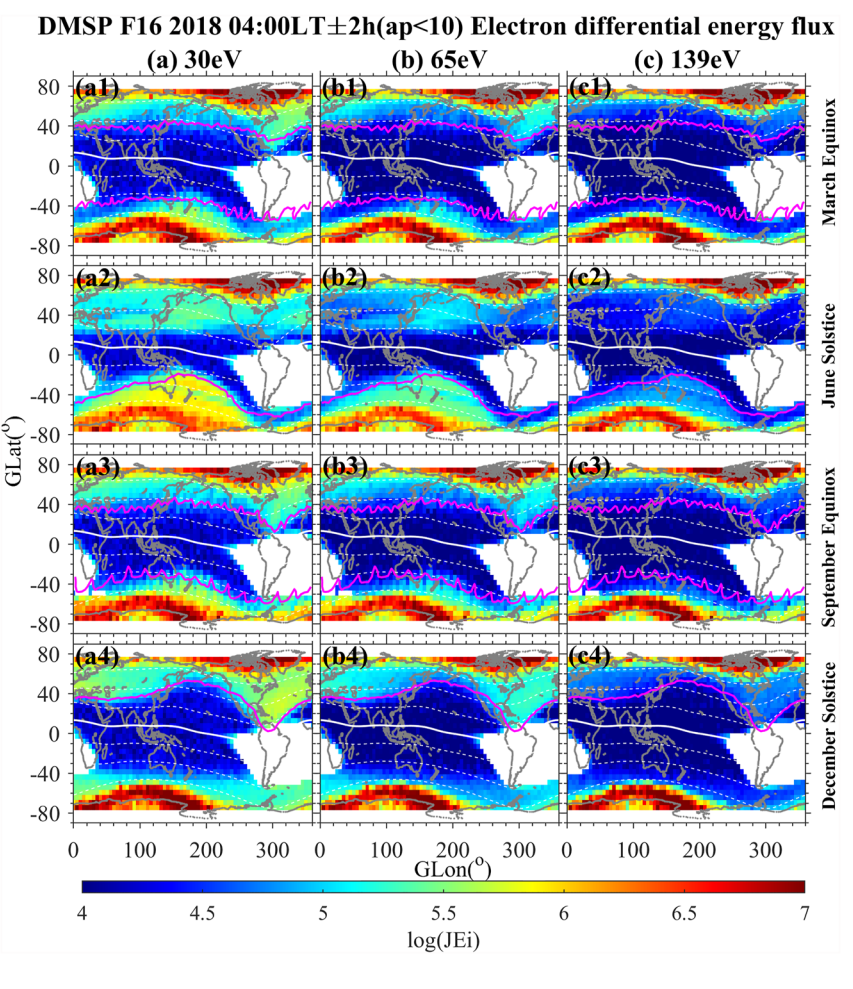


Figure 4. The same as Figure 3, but for 2018.

(Figure 6a1) and September Equinox (Figure 6a3) corresponded to the high electron density, regardless of NH and SH. The electron temperature is almost proportional to the electron density, and the distribution of the two is very consistent. The electron temperature enhancement region in the Southern Pacific sector around 200°E (the North American-Atlantic sector) in the June (December) Solstice (Figures 6a2 and 6a4) also corresponded to high electron density. This winter night amorous electron density variations at mid-latitudes have been well noticed in the F region ionospheric observations and explained as the consequence of plasmaspheric electron temperature elevation (Cai et al., 2022; Mikhailov et al., 2000; Richards et al., 2000). Thus, this positive correlation between electron density and temperature is not related to the electron cooling or heat capability effect but is more likely heating associated with CP. However, in the Eastern Indian Ocean sector around 120°E (the Eurasia sector) of the SH (NH), electron density was low and appeared to be inversely proportional to electron temperature.

The relationship between electron temperature and density is more complex in 2018 than in 2014. No matter what season in the NH (Figures 6b1, b3, and b4), the electron temperature enhancement regions with higher temperature in the North America-Atlantic sector correspond to low density, while the regions with lower temperature correspond to high density. The anti-correlation is still valid in the Eurasia sector. In the SH (Figures 6b1, 6b2, and 6b3), the electron temperature enhancement region corresponds to high density. The complex relationship between electron temperature and density at mid-low latitudes at the DMSP altitude confirms earlier studies suggesting the dependency of the relationship on seasons, local time, and solar activity (Su et al., 2015; Zhang & Holt, 2004; Zhang et al., 2004). Recently, Kil et al. (2022) also mentioned that the ionospheric temperature and density in the region affected by CPs on nightside were not simply anti-correlation. In the region with high ionospheric temperature and density, it is likely that excessive extra heating by CP plays an important role. The region with low density and high temperature could be understood in terms of the combined effects of the low electron

LIANG ET AL. 7 of 13

.com/doi/10.1029/2023JA031513 by Massachusetts Institute of Technolo, Wiley Online Library on [01/09/2023]

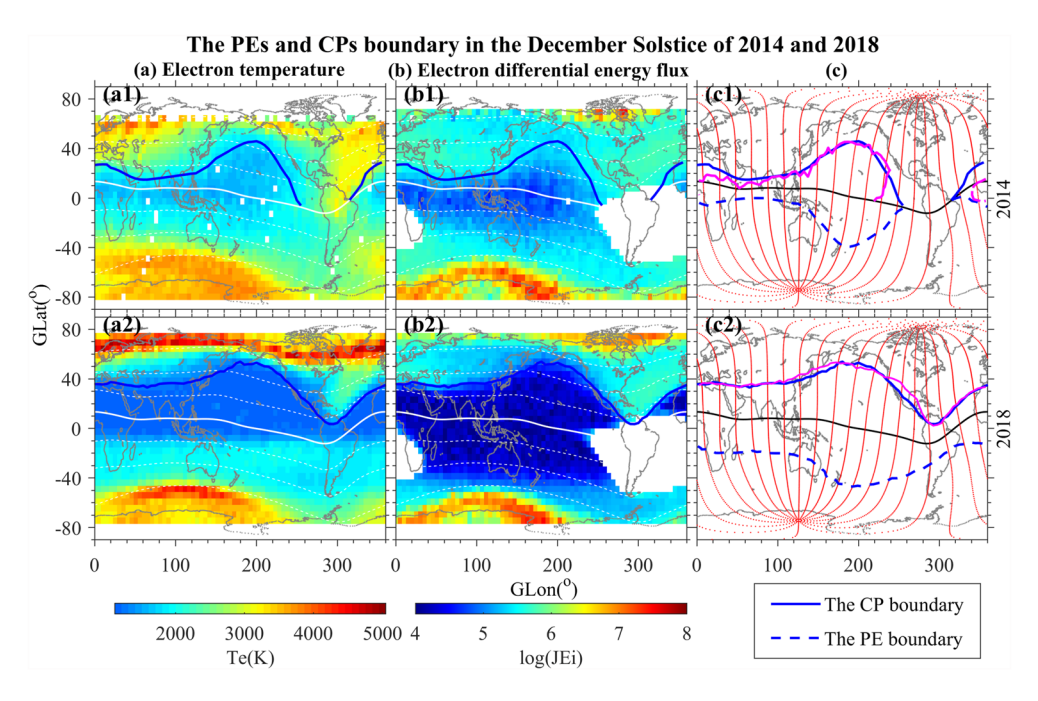


Figure 5. Comparison of the distribution of conjugate photoelectrons (CPs) and PEs in the December Solstice of 2014 and 2018 with electron temperature enhancement (a) and differential energy flux of 30 eV electron (b). And the influence of magnetic declination and tilted magnetic equator on the distribution of CPs and PEs (c).

density and a contribution from CPs. Variations of F2 region electron density at night can be very dynamic, depending not only on the topside thermal processes but more fundamentally on the F2 dynamics, including thermospheric wind influences. These electron density topics are beyond our main focus of the present study.

We conclude that the electron temperature enhancement at mid-low latitude in the night hemisphere may be contributed by PE heating from the conjugate sunlit hemisphere, and under certain conditions, some of the regions may be affected additionally by the low electron density. DMSP measurements of electron differential

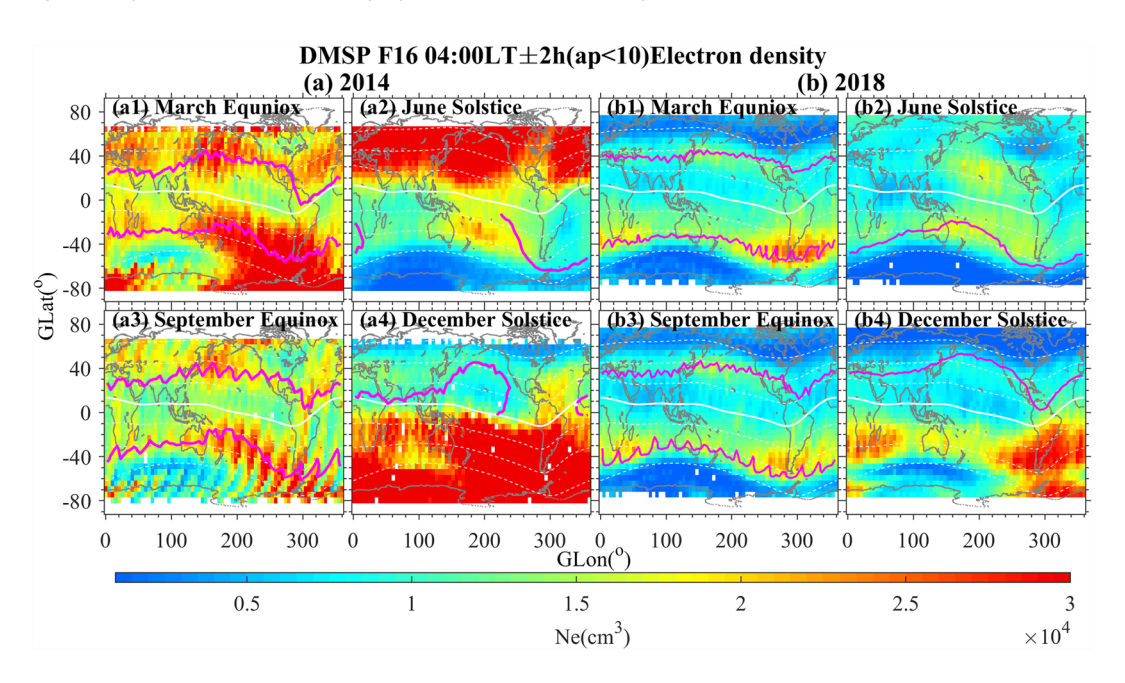


Figure 6. Electron density during geomagnetic quiet times in (a) 2014 and (b) 2018. The white and magenta lines are the same as Figure 3.

LIANG ET AL. 8 of 13

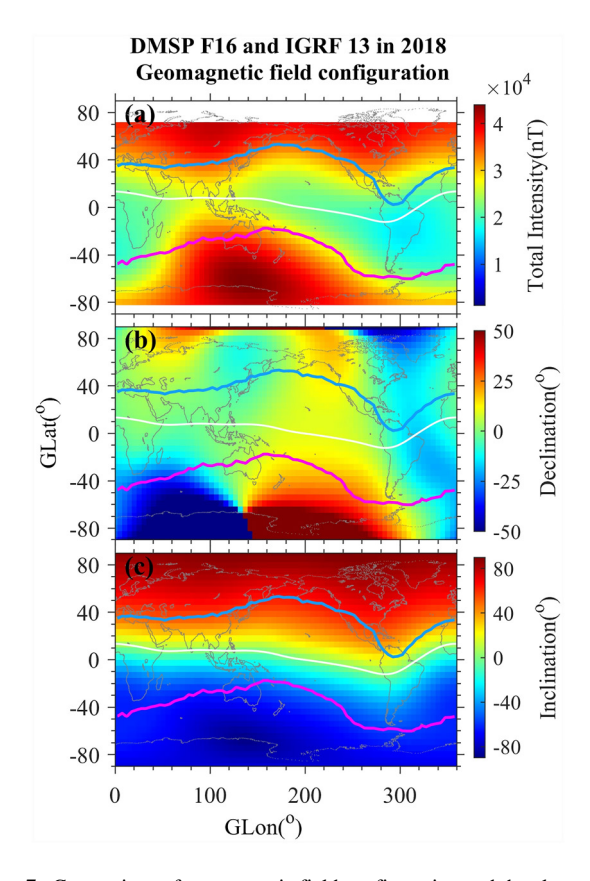


Figure 7. Comparison of geomagnetic field configuration and the electron temperature enhancement distribution in 2018. Figures (a–c) show the total magnetic field intensity measured by Defense Meteorological Satellite Program F16, the magnetic declination, and the inclination obtained by IGRF13 in 2018. The blue (NH) and magenta (SH) lines are the boundaries of the electron temperature enhancement region in the December Solstice of 2018, and the white line is the magnetic latitude line of 0°.

flux provide an important global distribution of the PEs in both the sunlit and conjugate hemispheres. Moreover, the equatorward extension of the high electron temperature zone in the Solstice of 2014 appears to be associated with a joint impact of PEs in both the local and the conjugate sunlit hemispheres. The mix of local and remote impacts varies as a function of latitude.

4.2. What Affects the Distribution of Electron Temperature Enhancement?

As discussed above, CPs contribute significantly to electron temperature enhancement. Therefore, it can be further inferred that the magnetic field configuration and the terminator distribution may have a great impact on the distribution of these CPs.

The electron temperature enhancement distribution is related to the geomagnetic field configuration, as shown in Figure 7. Figure 7a reveals the relationship between the geomagnetic intensity and electron temperature enhancement distribution (magenta and blue lines) in the winter hemisphere in 2018. The longitudinal and latitudinal structure of the geomagnetic intensity deviates slightly from the blue (magenta) line boundary of the electron temperature enhancement region in the NH (SH). The Northern Atlantic (Southern Oceania) sector has a magnetic declination that is more west (east) and has a more pronounced westward (eastward) electron temperature enhancement morphology in the NH (SH) winter, as shown in Figure 7b. A comparison between the Eastern Asia and Northern Atlantic sectors in Figure 7b shows that the enhancement region with a more west magnetic declination in the Northern Atlantic sector has a considerably higher temperature. According to Figure 7c, the enhancement region with a larger north (south) inclination in the Atlantic and Eastern Asia (Southern Oceania) sectors can extend to lower latitudes in the NH (SH) winter.

Taking 22 December 2018 as an example, we divided the NH into four sectors with different geomagnetic field conditions. In each sector, we examined that the satellite flew over 40°N (while the terminator swept over the 24.74°S point), which would be under the influence of the PE from the conjugate hemisphere, to discuss further the modulation effect of the geomagnetic field on the distribution of electron temperature enhancement at mid-low latitude.

Figures 8a and 8b reveal the physical schematic diagram of CPs distribution in four sectors modulated by geomagnetic configuration. The magenta star (green star) is the CP precipitation (PE generated) boundary. The CP precipitation boundary (magenta star) is significantly closer to the magnetic equator at the west magnetic declination than the intersection (white dot) of the meridian and terminator in Figure 8a1. Comparing Figures 8a1 and 8a2, the magnetic point with a more west magnetic declination makes the corresponding magnetic conjugate point (i.e., the CP precipitated boundary) closer to the magnetic equator. However, the CP precipitation boundary is far from the magnetic equator at the east magnetic declination in Figure 8b2. The point with a more east magnetic declination makes the CP precipitation boundary further away from the magnetic equator (Figure 8b1). Moreover, the magnetic equator closer to the NH (SH) on the meridian in Figure 8a2 (Figure 8a1) also makes the CP precipitation boundary closer to (further away from) the magnetic equator. Figure 6c further illustrates that the more west magnetic declination and the magnetic equator closer to the NH make the CPs (PEs) distribution closer to the magnetic equator, while the more east magnetic declination is further away from the magnetic equator. Therefore, the CPs precipitation distribution extends closer to the magnetic equator in the Northern Atlantic sector, shrinks back to middle magnetic latitudes in the Eurasia sector, and even to high magnetic latitudes in the Pacific sector. That is, the magnetic declination and the position of magnetic equator govern the morphology of the electron temperature enhancement region. Kil et al. (2020) also examined the influence of magnetic declination on CPs. At west magnetic declination, the 130.4 nm anomalous emission in the NH is produced by the PEs created at an earlier time in the SH. Conversely, it comes from PEs production at a later time at the west magnetic declination.

LIANG ET AL. 9 of 13

from https://agupubs.onlinelibrary.wiley.com/doi/10.1029/2023J A031513 by Massachusetts Institute of Technolo, Wiley Online Library on [01/09/2023]. See the Terms and Conditions (https://onlineli

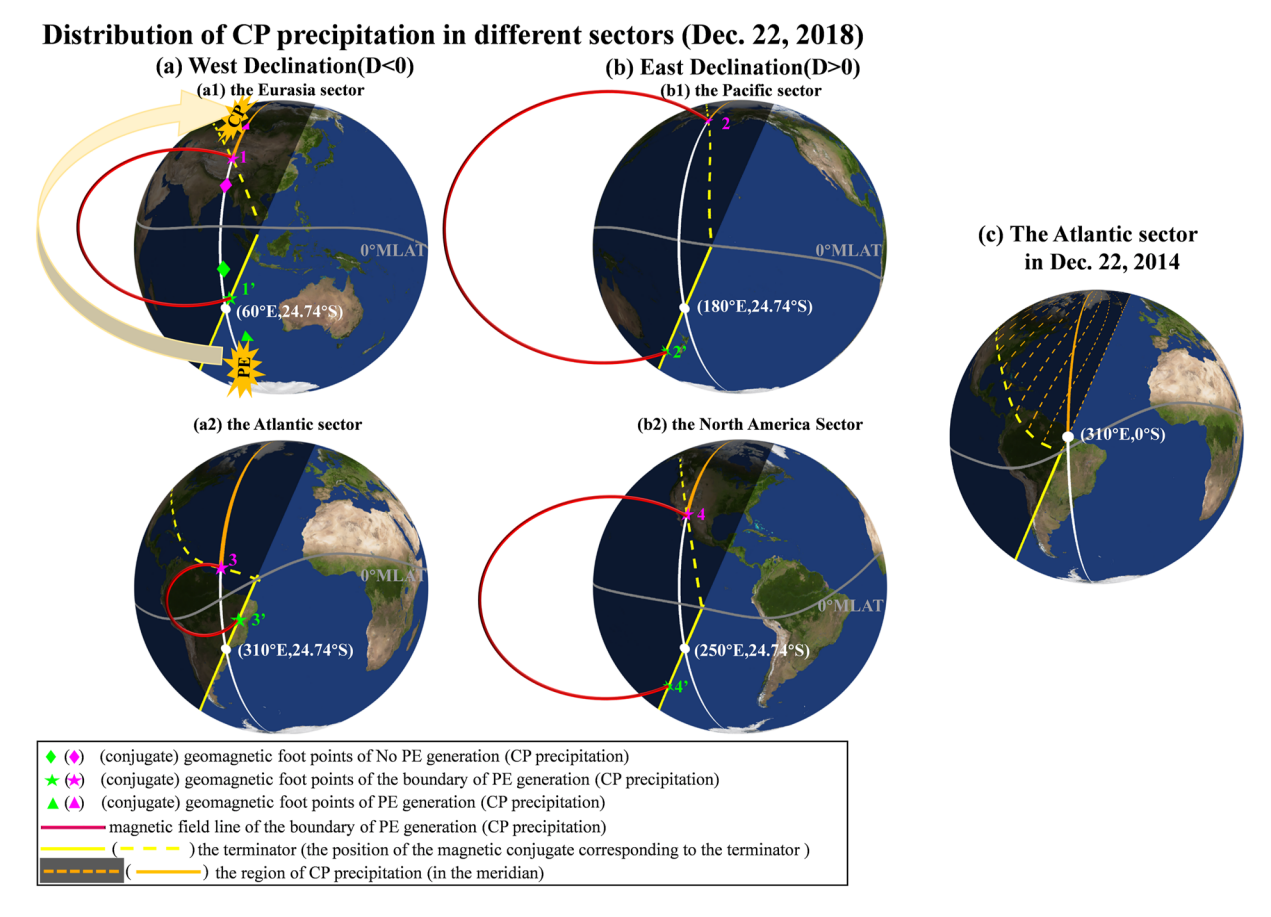


Figure 8. Schematic of the distribution of conjugate photoelectron precipitation in different sectors on 22 December 2018 (Panels (a and b)) and the crossing equator structure formation on 22 December 2014 (Panel (c)). Figures are the Defense Meteorological Satellite Program F16 flew through 40°N at (a1) 90°E, (a2) and (c) 310°E, (b1) 180°E, and (b2) 250°E meridian. The white dots are the intersection of the terminator (junction of light and dark areas at position of SZA = 100°) and meridians (white lines). Points 1 and 1', 2 and 2', and 3 and 3' are magnetic conjugate foot points, respectively.

As discussed earlier, at least two factors contribute to the intensity of the electron temperature enhancement region: the CP flux and the electron density. The flux of CP (Φ_c) is affected by the magnetic field line length (L_{co}) and intensities between the PE generated point (B_o) and CP precipitated point (B_c). For $B_c \ge B_o$, $\Phi_c = \Phi_o$; otherwise, $\Phi_c < \Phi_o$ when considering pitch angles (but not loss) (Solomon et al., 2020). The longer the magnetic field lines, the more losses the CPs incur in the movement process (Kakinami et al., 2010). The magnetic field line length between the two magnetic conjugate points (L_{co}) has $L_{44'} > L_{11'} > L_{33'}$ in Figures 8b2, 8a1, and 8a2, even though the magnetic field intensity is $B_{1(3)(4)} > B_{1'(3')(4')}$. Furthermore, $B_2 < B_{2'}$ and $L_{22'} >> L_{44'}$ (11')(33'), which even reaches the plasmaspheric boundary in Figure 8b1. These conditions may result in the maximum CP flux in the Northern Atlantic sector. On the other hand, this sector has a relatively low electron density compared with other sectors. Therefore, this region has the highest electron temperature.

However, the west magnetic declination makes the CP precipitation region further away from the magnetic equator in the SH in the June Solstice. The electron temperature enhancement region can shrink to higher latitudes, owing to the west magnetic declination and close to the magnetic equator of the NH in the South American sector. The east magnetic declination and the magnetic equator almost parallel to the geographical equator result in the electron temperature enhancement region being close to the magnetic equator in the Southern Oceania sector. Because the terminator almost coincides with the meridian at mid-low latitudes in the Equinox, the west (east) magnetic declination also causes the CP precipitation boundary to be closer to the magnetic equator in the NH (SH). However, the CP precipitation boundary is at a considerably higher latitude than in the December (June) Solstice, resulting in a longer magnetic field line. As a result, the latitudinal extension and intensity of electron temperature enhancement in the North American-Atlantic (Southern Oceania) sector in the Equinox are weaker than in the Solstice.

LIANG ET AL. 10 of 13

The above discussions are all based on a solar minimum year for 2018. Electron temperature enhancement in a solar maximum year for 2014 (Panel (a) in Figure 2) had a wider latitude-longitude span and higher temperature than that in 2018 (Panel (b) in Figure 2). Especially in the December Solstice of 2014 (Figure 2a4), the electron temperature enhancement regions exhibited substantial equatorward extension. The modulation effect of the geomagnetic field on the flux of CPs precipitation is the same regardless of a solar maximum or minimum year. The electron temperature enhancement distribution in 2014 has been discussed in Section 4.1, perhaps mainly due to the solar LT effect. The LT of DMSP F16 satellite in 2014 was 1 hr later than that in 2018 at all latitudes. Therefore, when the satellite flew to a fixed latitude in 2014 and 2018, on the one hand, the intersection of the meridian and the terminator would be closer to the magnetic equator in 2014 than that in 2018 (i.e., the white point in Figures 8a and 8b). Even the intersection was above the magnetic equator in the North Atlantic in 2014 (Figure 8c). On the other hand, the west magnetic declination made the CP boundary closer to the magnetic equator in 2014 than in 2018, and the east magnetic declination was the opposite. Figure 6c further shows the PE (light blue dotted line) and CP (light blue line) distributions, which further reveals the LT influence on the electron temperature enhancement distribution. There is a wider longitude-latitude span under LT of DMSP F16 satellite in 2014 in Figure 6c1 than Figure 6c2. Higher electron temperature in the electron temperature enhancement region in 2014 may not be affected by electron cooling because it corresponded to a higher electron density than in 2018. It may be the superimposing effect of EUV radiation and LT. (a) The LT in 2014 was closer to the dawn side, and then the heating effect was more pronounced. (b) Compared with the solar minimum year, the 2 times increase in EUV radiation in the solar maximum year leads to an increase in the photoionization rate (Lean et al., 2003), which in turn causes an increase in the flux of PEs (Richards & Torr, 1985). Moreover, the electron temperature during the high solar activity is ~800 K higher than that during the low solar activity by DMSP F10-15 satellites observations on nightside (Truhlik et al., 2009). The flux of PE increases leads to the increase of CP reaching the nightside hemisphere in the high solar activity (Kakinami et al., 2010). As a result, the electron temperature enhancement in 2014 is more notable than that in 2018.

5. Conclusions

We investigated the global distribution of electron temperature enhancement in the solar maximum (2014) and minimum (2018) years using DMSP F16 electron temperature data observed under a geomagnetic quiet condition. The major features of the electron temperature enhancement distributions are:

- 1. In the December Solstice, the electron temperature enhancement was identified at night in winter midlatitudes in the Eurasian sector and could be extended equatorward into equatorial latitudes in the Northern Atlantic sector. In the solar maximum year, it went further equatorward;
- 2. In the June Solstice, however, the enhancement zone was in the Southern Oceania sector, not as low in magnetic latitudes as in the December Solstice but similarly more equatorward for a solar maximum than minimum year;
- 3. In the Equinox, electron temperature enhancement occurred both in the NH and SH; however, they are not as noticeable as the electron temperature enhancement in the Solstice.

The distribution of low-energy electrons (<100 eV) precipitation at mid-low latitudes is consistent with that of electron temperature enhancement. These low-energy electrons at mid-low latitudes, which may be the source of the electron temperature enhancement, are likely from the CPs originated in the sunlit hemisphere. At equatorial latitudes, these enhancements are likely local PEs. If the west (east) magnetic declination is larger or the magnetic equator is closer to the SH (NH), the CP precipitation boundary in the NH (SH) is aligned more toward the magnetic equator, and vice versa. Thus, the magnetic declination and tilted magnetic equator can control the electron temperature enhancement distribution. The magnetic field line length and intensity can affect the flux of CPs precipitated in the conjugate hemisphere and then affect the temperature and density in the electron temperature enhancement region. The electron temperature enhancement distribution is slightly different in different seasons owing to the different locations of the terminator. We also note that some of the high electron temperature enhancement zone appears to correspond with low electron density, especially at solar minimum, where low electron density and the associated low cooling rates yield high electron temperature.

Data Availability Statement

The DMSP data can be downloaded at https://www.ncei.noaa.gov/data/dmsp-space-weather-sensors/access/. The ap data can be downloaded at https://cdaweb.gsfc.nasa.gov/. The IGRF13 code can be obtained from https://www.ngdc.noaa.gov/IAGA/vmod/igrf.html.

LIANG ET AL. 11 of 13

Acknowledgments

The work in China was supported by the National Natural Science Foundation of China (Grants 41831073, 42120104003), and the International Partnership Program of Chinese Academy of Sciences (Grant 183311KYSB20200003). SRZ acknowledges funding support from the U.S. NSF (Grants AGS-1952737, AGS-2033787, AGS-2149698), and U.S. ONR (Grant N00014-23-1-2160). We thank the NOAA FTP for making available the DMSP data, the OMNI database for offering the 3-h ap index data, and the IAGA Working Group V-MOD for making available the IGRF13 code.

References

- Anderson, P. C., Rich, F. J., & Borisov, S. (2018). Mapping the South Atlantic anomaly continuously over 27 years. *Journal of Atmospheric and Solar-Terrestrial Physics*, 177, 237–216. https://doi.org/10.1016/j.jastp.2018.03.015
- Bilitza, D., Truhlik, V., Richards, P., Abe, T., & Triskova, L. (2007). Solar cycle variations of mid-latitude electron density and temperature: Satellite measurements and model calculations. *Advances in Space Research*, 39(5), 779–789. https://doi.org/10.1016/j.asr.2006.11.022
- Brace, L. H., Spencer, N. W., & Carignan, G. R. (1963). Ionosphere electron temperature measurements and their implications. *Journal of Geophysical Research*, 68(19), 5397–5412. https://doi.org/10.1029/j.2156-2202.1963.tb00020.x
- Burke, W. J., Sagalyn, R. C., & Kanal, M. (1979). Observed heating effects of conjugate photoelectrons. *Planetary and Space Science*, 27(5), 583–591. https://doi.org/10.1016/0032-0633(79)90156-9
- Cai, Y., Yue, X., Wang, W., Zhang, S.-R., Liu, H., Lei, J., et al. (2022). Ionospheric topside diffusive flux and the formation of summer night-time ionospheric electron density enhancement over millstone hill. Geophysical Research Letters, 49(4), e2021GL097651. https://doi.org/10.1029/2021gl097651
- Carlson, H. C. (1966). Ionospheric heating by magnetic conjugate-point photoelectrons. Journal of Geophysical Research, 71(1), 195–199. https://doi.org/10.1029/jz071i001p00195
- Carlson, H. C. (1968). Most recent studies of low latitude effects due to conjugate location heating. Radio Science, 3(7), 668–673. https://doi.org/10.1002/rds196837668
- Carru, H., Petit, M., & Waldteufel, P. (1967). Mesures de températures électroniques et ioniques par diffusion incohérente. *Journal of Atmospheric and Terrestrial Physics*, 29(4), 351–366. https://doi.org/10.1016/0021-9169(67)90018-9
- Chao, C. K., Su, S. Y., & Yeh, H. C. (2003). Presunrise ion temperature enhancement observed at 600 km low- and mid-latitude ionosphere. Geophysical Research Letters, 30(4), 1187. https://doi.org/10.1029/2002GL016268
- Daniel, M. O., Ernest, H., Rich, F. J., Gentile, L. C., Wilson, G. R., & John, S. M. (2014). The DMSP space weather sensors data archive listing (1982–2013) and file formats descriptions. Tech. Rep AFRL-RV-PS-TR-2014-0174. Air Force Geophys. Lab., Hanscom Air Force Base.
- Delorey, D. E., Pruneau, P. N., & Parsons, C. M. (1989). Database development for the DMSP SSIES experiment. Tech. Rep. GL-TR-89-0066. Air Force Geophys. Lab., Hanscom Air Force Base.
- Duboin, M. L., Lejeune, G., Petit, M., & Weill, G. (1968). Excitation of the oxygen lines and ionospheric heating by conjugate photoelectrons. Journal of Atmospheric and Terrestrial Physics, 30(2), 299–304. https://doi.org/10.1016/0021-9169(68)90084-6
- Evans, J. V. (1967). Midlatitude electron and ion temperatures at sunspot minimum. Planetary and Space Science, 15(10), 1557–1570. https://doi.org/10.1016/0032-0633(67)90089-x
- Evans, J. V. (1968). Sunrise behavior of the F layer at midlatitudes. *Journal of Geophysical Research*, 73(11), 3489–3504. https://doi.org/10.1029/
- ja073i011p03489 Evans, J. V., & Gastman, I. J. (1970). Detection of conjugate photoelectrons at millstone hill. *Journal of Geophysical Research*, 75(4), 807–815.
- https://doi.org/10.1029/ja075i004p00807

 Geisler, J. E., & Bowhill, S. A. (1965). Exchange of energy between the ionosphere and the protonosphere. *Journal of Atmospheric and Terrestrial Physics*, 27(11–12), 1119–1146. https://doi.org/10.1016/0021-9169(65)90073-5
- Green, B. S. (2001). Validation and assessment of DMSP electron temperatures in the topside ionosphere. AFIT/GAP/ENP/01M-03. Air Force Institute of Technology.
- Hanson, W. B. (1963). Electron temperatures in the upper atmosphere. Space Research, 5, 282-302.
- Hardy, D. A., Yeh, H. C., Schmitt, L. K., Schumaker, T. L., Gussenhoven, M. S., Huber, A., et al. (1984). Precipitating electron and ion detectors (SSJ/4) for block 5D/flights 4-10 DMSP satellites: Calibration and data presentation. Tech. Rep AFGL-TR-84-0317. Air Force Geophys. Lab., Hanscom Air Force Base.
- Kakinami, Y., Balan, N., Liu, J. Y., & Oyama, K. I. (2010). Predawn ionospheric heating observed by Hinotori satellite. *Journal of Geophysical Research*, 115(A1), A01304. https://doi.org/10.1029/2009ja014334
- Kil, H., Paxton, L. J., & Schaefer, R. K. (2022). Simultaneous detection of signatures of conjugate photoelectrons in the ionosphere and thermosphere. *Journal of Geophysical Research: Space Physics*, 127(5), e2021JA030121. https://doi.org/10.1029/2021JA030121
- Kil, H., Schaefer, R. K., Paxton, L. J., & Jee, G. (2020). The far ultraviolet signatures of conjugate photoelectrons seen by the Special Sensor Ultraviolet Spectrographic Imager. *Geophysical Research Letters*, 47(1), e2019GL086383. https://doi.org/10.1029/2019GL086383
- Kwei, M. W. (1967). Presunrise effects due to conjugate region photoelectrons. (No. NASA-CR-89273).
- Kwei, M. W., & Nisbet, J. S. (1966). Presunrise heating of the ambient electrons in the ionosphere due to conjugate point photoelectrons. (No. NASA-CR-83671).
- Kwei, M. W., & Nisbet, J. S. (1968). Presunrise heating of the ionosphere at Arecibo due to conjugate point photoelectrons. *Radio Science*, 3(7), 674–679. https://doi.org/10.1002/rds196837674
- Lean, J. L., Warren, H. P., Mariska, J. T., & Bishop, J. (2003). A new model of solar EUV irradiance variability 2. Comparisons with empirical models and observations and implications for space weather. *Journal of Geophysical Research*, 108(A2), 1059. https://doi.org/10.1029/2001ja009238
- Meng, C. I. (1976). Simultaneous observations of low-energy electron precipitation and optical auroral arcs in the evening sector by the DMSP 32 satellite. *Journal of Geophysical Research*, 81(16), 2771–2785. https://doi.org/10.1029/ja081i016p02771
- Mikhailov, A. V., Förster, M., & Leschinskaya, T. Y. (2000). On the mechanism of the post-midnight winter N mF2 enhancements: Dependence on solar activity. *Annales Geophysicae*, 18(11), 1422–1434. https://doi.org/10.1007/s00585-000-1422-y
- Mukai, T., Kondo, Y., & Hirao, K. (1979). Rocket observation of conjugate photoelectrons in the predawn ionosphere. *Planetary and Space Science*, 27(1), 31–38. https://doi.org/10.1016/0032-0633(79)90144-2
- Nagy, A. F., & Banks, P. M. (1970). Photoelectron fluxes in the ionosphere. *Journal of Geophysical Research*, 75(31), 6260–6270. https://doi.org/10.1029/JA075i031p06260
- Nagy, A. F., Fontheim, E. G., Stolarski, R. S., & Beutler, A. E. (1969). Ionospheric electron temperature calculations including protonospheric and conjugate effects. *Journal of Geophysical Research*, 74(19), 4667–4676. https://doi.org/10.1029/ja074i019p04667
- Newell, P. T., Feldstein, Y. I., Galperin, Y. I., & Meng, C. I. (1996). Morphology of nightside precipitation. *Journal of Geophysical Research*, 101(A5), 10737–10748. https://doi.org/10.1029/95JA03516
- Newell, P. T., Ruohoniemi, J. M., & Meng, C. I. (2004). Maps of precipitation by source region, binned by IMF, with inertial convection streamlines. *Journal of Geophysical Research*, 109(A10), A10206. https://doi.org/10.1029/2004JA010499
- Oyama, K. I., Abdu, M. A., Balan, N., Bailey, G. J., Watanabe, S., Takahashi, T., et al. (1997). High electron temperature associated with the prereversal enhancement in the equatorial ionosphere. *Journal of Geophysical Research*, 102(A1), 417–424. https://doi.org/10.1029/96JA02705
- Rao, N. B. C., & Maier, E. J. R. (1970). Photoelectron flux and protonospheric heating during the conjugate point sunrise. *Journal of Geophysical Research*, 75(4), 816–824. https://doi.org/10.1029/ja075i004p00816

LIANG ET AL. 12 of 13

- Rich, F. J. (2001). Description of DMSP/SSM data for ionospheric/magnetospheric research.
- Richards, P. G., Buonsanto, M. J., Reinisch, B. W., Holt, J., Fennelly, J., Scali, J. L., et al. (2000). On the relative importance of convection and temperature on the behavior of the ionosphere in North America during January, 6–12, 1997. *Journal of Geophysical Research*, 105(A6), 12763–12776. https://doi.org/10.1029/1999JA000253
- Richards, P. G., & Torr, D. G. (1985). The altitude variation of the ionospheric photoelectron flux: A comparison of theory and measurement. Journal of Geophysical Research, 90(A3), 2877–2884. https://doi.org/10.1029/ja090ia03p02877
- Schunk, R. W., & Nagy, A. F. (1978). Electron temperatures in the F region ionosphere: Theory and observations. Reviews of Geophysics and Space Physics, 16(3), 355–399. https://doi.org/10.1029/RG016i003p00355
- Shawhan, S. D., Block, L. P., & Falthammar, C. G. (1970). Conjugate photoelectron impact ionization. *Journal of Atmospheric and Terrestrial Physics*, 32(12), 1885–1900. https://doi.org/10.1016/0021-9169(70)90085-1
- Solomon, S. C., Andersson, L., Burns, A. G., Eastes, R. W., Martinis, C., McClintock, W. E., & Richmond, A. D. (2020). Global-scale observations and modeling of far-ultraviolet airglow during twilight. *Journal of Geophysical Research: Space Physics*, 125(3), e2019JA027645. https://doi.org/10.1029/2019JA027645
- Su, F., Wang, W., Burns, A. G., Yue, X., & Zhu, F. (2015). The correlation between electron temperature and density in the topside ionosphere during 2006–2009. Journal of Geophysical Research: Space Physics, 120(12), 10724–10739. https://doi.org/10.1002/2015JA021303
- Su, Y. J., Caton, R. G., Horwitz, J. L., & Richards, P. G. (1999). Systematic modeling of soft-electron precipitation effects on high-latitude F region and topside ionospheric upflows. *Journal of Geophysical Research*, 104(A1), 153–156. https://doi.org/10.1029/1998ja900068
- Truhlik, V., Bilitza, D., & Triskova, L. (2009). Latitudinal variation of the topside electron temperature at different levels of solar activity. Advances in Space Research, 44(6), 693–700. https://doi.org/10.1016/j.asr.2009.04.029
- Watanabe, S., Oyama, K. I., & Abdu, M. A. (1995). Computer simulation of electron and ion densities and temperatures in the equatorial F region and comparison with Hinotori results. *Journal of Geophysical Research*, 100(A8), 14581–14590. https://doi.org/10.1029/95JA01356
- Zhang, S. R., & Holt, J. M. (2004). Ionospheric plasma temperatures during 1976–2001 over millstone hill. Advances in Space Research, 33(6), 963–969. https://doi.org/10.1016/j.asr.2003.07.012
- Zhang, S. R., Holt, J. M., Zalucha, A. M., & Amory-Mazaudier, C. (2004). Midlatitude ionospheric plasma temperature climatology and empirical model based on Saint Santin incoherent scatter radar data from 1966 to 1987. *Journal of Geophysical Research*, 109(A), 11311. https://doi.org/10.1029/2004ja010709

LIANG ET AL. 13 of 13